RSC Advances

PAPER

View Article Online
View Journal | View Issue

Cite this: *RSC Adv.*, 2026, **16**, 29434

Z-Scheme $CoFe_2O_4$/g-C_3N_4/MWCNT catalyst for the degradation of organic pollutants: electrochemical evaluation and HPLC analysis of the intermediates

Garima Rana,[a] Ritesh Verma,[b] Eman A. Alabdullkarem,[c] Subha Krishna Rao,[d] Kun-Yi Andrew Lin,[e] Suresh Ghotekar *[f] and Ankush Chauhan *[f]

In this work, a ternary $CoFe_2O_4$/g-C_3N_4/MWCNT (CGC4) nanocomposite (NC) was successfully produced through a sol–gel auto-combustion approach, followed by calcination. It was evaluated for its efficacy in the visible-light-driven photocatalytic decomposition of RhB. XRD, FESEM–EDS, XPS, FTIR spectroscopy, and zeta potential measurements of the structure, morphology, and surface chemistry showed that a well-integrated hetero-structured nanocomposite was formed with better crystallinity, interfacial coupling, and surface activity. The CGC4 photocatalyst showed improved photocatalytic performance, degrading 84.1% of RhB in 180 minutes and exhibiting a much higher pseudo-first-order rate constant of 1.5×10^{-4} s^{-1} than pure $CoFe_2O_4$ and binary composites. The optimization studies showed that the catalyst amount, initial dye concentration, and pH significantly affected the degradation efficiency. The scavenger tests revealed that superoxide radicals and photogenerated holes were the most reactive species. High-performance liquid chromatography (HPLC) analysis showed that rhodamine B (RhB) was broken down into less harmful intermediates without creating toxic by-products. The improved photocatalytic performance is due to the Z-scheme heterojunction, the conductive multi-walled carbon nanotube (MWCNT) network, and the synergistic interaction of the components, which enhance charge separation. This study shows that $CoFe_2O_4$/g-C_3N_4/MWCNT NCs can serve as effective visible-light-responsive photocatalysts for wastewater treatment. Electrochemical analysis showed that CGC2 had the highest specific capacitance of 6.407 F g^{-1}. The CGC2 samples also exhibited the highest energy density and stored charge at a scan rate of 0.08 V s^{-1}. The enhanced performance was associated with the synergistic interaction between the conductive network of MWCNTs and the electroactive $CoFe_2O_4$ nanoparticles. The enhanced performance is also well supported by the Nyquist and Randles–Sevcik plots. Thus, in CGC2 samples, the synergistic effect enabled efficient electron transport and ion accessibility.

Received 10th March 2026
Accepted 12th May 2026

DOI: 10.1039/d6ra02055k

rsc.li/rsc-advances

1. Introduction

Water is a major resource for all living organisms; however, despite its importance, there are alarming concerns about water pollution affecting them directly or indirectly. The contaminants of great concern and the emerging contaminants arising from domestic, agricultural, and industrial wastes, which may also be present at minute concentrations undetectable without sophisticated analytical techniques, pose health hazards upon prolonged exposure.[1,2] Dyes and pigments are widely used in diverse industries as colorants and for staining in analytical and biological laboratories. Rhodamine B (RhB) is one such dye used in the manufacturing of paints, textiles, and leathers as a colorant and for staining in laboratories. However, the discharge of RhB into the environment causes water pollution due to its high toxicity, carcinogenic potential, neurotoxicity, and adverse effects on aquatic species.[3,4] It is highly stable, with low degradation, and remains persistent in wastewater.[5] Various techniques, such as advanced oxidation processes, electrocatalysis, adsorption, photocatalysis, and membrane filtration, are used to remove or degrade RhB.[6–10] Among these

[a]Department of Physics, Bahra Research Innovation & Knowledge Cluster (BRIKC), Rayat Bahra University, Greater Mohali 140103, Punjab, India
[b]Department of Physics, Graphic Era (Deemed to Be) University, Dehradun, Uttarakhand, India
[c]Department of Chemistry, College of Science, King Saud University, P. O. Box 2455, Riyadh 11451, Saudi Arabia
[d]Centre for Nanoscience and Nanotechnology, International Research Centre, Sathyabama Institute of Science and Technology, Chennai 600119, India
[e]Department of Environmental Engineering & Innovation and Development Center of Sustainable Agriculture, National Chung Hsing University, Taichung, Taiwan
[f]Centre for Herbal Pharmacology and Environmental Sustainability, Chettinad Hospital and Research Institute, Chettinad Academy of Research and Education, Kelambakkam 603103, Tamil Nadu, India. E-mail: ghotekarsuresh7@gmail.com; ankushchauhan18@gmail.com

techniques, photocatalysis is an environmentally friendly method for the photodegradation of organic pollutants because it operates on a simple mechanism: irradiating a semiconductor with light of energy greater than its bandgap.[11] Further, the electron–hole pairs are generated, and the electrons are excited from the valence band to the conduction band of the semiconductor. The reactive holes in the valence band oxidize H_2O and OH^- species, forming hydroxyl radicals, whereas electrons in the conduction band react with surface oxygen species to form superoxide radicals ($^{\bullet}O_2^-$), which further degrade the pollutants.[12–14] The direct Z-scheme charge carrier transmission pathway preserves photogenerated electrons with strong reduction capabilities in the conduction band (CB) of PC I and holes with strong oxidation capabilities in the valence band (VB) of PC II, while the photogenerated electrons in the CB of PC II and holes in the VB of PC I, possessing inferior redox power, undergo recombination. Consequently, a Z-scheme photocatalyst possesses robust redox capabilities for facilitating photocatalytic processes, together with spatially distinct reductive and oxidative active sites. Furthermore, a semiconductor photocatalyst with a low bandgap may be chosen to develop direct Z-scheme photocatalysts, thereby expanding the light-harvesting spectrum.[15]

Cobalt ferrite ($CoFe_2O_4$) nanoparticles act as a spinel ferromagnetic semiconductor with excellent magnetic, electronic, and optical properties, but their small bandgap of around 1.33 eV results in a fast recombination of electrons and holes and incomplete spectrum adsorption.[16] However, it has been reported that $CoFe_2O_4$, in combination with various semiconductor and conductive materials, acts as an excellent photocatalyst for the decomposition of organic contaminants. There are some examples of such composites: $CoFe_2O_4$ decorated g-C_3N_4 nanosheets showing 93.96% degradation of Methylene blue (MB) dye under visible light,[17] $CoFe_2O_4$/Ag-MWCNT nanocomposite,[18] CuO/$CoFe_2O_4$/MWCNT ternary nanocomposite,[19] $CoFe_2O_4$/MWCNT,[20] cobalt ferrite anchored g-C_3N_4 nanocomposite,[21] *etc.* In recent years, graphitic carbon nitride (g-C_3N_4) has emerged as one of the most promising photocatalysts, owing to its high chemical and thermal stability, low toxicity, ease of synthesis, and strong adsorption.[22,23] It exhibits an optical bandgap of ~2.85 eV, making it an excellent candidate for photocatalytic reactions. However, its high recombination rate of photogenerated charge carriers and its limited spectral response range limit its practical application in photocatalysis.[24–26] The combination of g-C_3N_4 with semiconductors to form composites demonstrates efficient photocatalyst formation. Li *et al.* reported a black phosphorus/red phosphorus (BP/RP)-g-C_3N_4/SiO_2 heterojunction that showed a significant enhancement in photocatalytic efficacy, achieving 90% degradation of RhB under simulated solar radiation within 26 min.[27] Recently, several nanocomposites with g-C_3N_4 have been reported to have excellent photocatalytic properties for the degradation of organic pollutants, for example, graphitic carbon nitride/carbon nanotube/Bi_2WO_6,[28] g-C_3N_4/MWCNTs/Au,[29] g-C_3N_4-functionalized MWCNT,[30] and lanthanum-doped copper ferrite/graphitic carbon nitride composites.[31] Several studies have demonstrated that $CoFe_2O_4$/g-C_3N_4 nanocomposites with integrated Z-scheme heterojunctions serve as efficient photocatalysts. The $CoFe_2O_4$/g-C_3N_4 heterojunctions, due to their precise alignment in the valence band (VB) and conduction band (CB), may facilitate slower recombination under light irradiation.[16,32,33] Haider *et al.* fabricated a Z-scheme Bi_2WO_6/KCN heterojunction towards efficient photocatalytic degradation of tetracycline hydrochloride. The degradation efficiency of tetracycline hydrochloride could reach 87% within 20 min under optimal conditions. The enhanced photocatalytic efficacy of Bi_2WO_6/KCN is ascribed to its Z-scheme heterojunction construction, which markedly diminishes the recombination of photogenerated electron and hole (e^-/h^+) pairs.[34] Hence, in the present study, we report the synthesis of the ternary $CoFe_2O_4$/g-C_3N_4/MWCNT nanocomposite with enhanced photocatalytic and electrochemical activity. Specifically, the main aim of this study is to synthesize a ternary $CoFe_2O_4$/g-C_3N_4/MWCNT nanocomposite *via* calcination, analyze the degradation pathway using HPLC, and assess the impact of g-C_3N_4 and MWCNT on the structural, morphological, electrochemical, and photocatalytic degradation of RhB.

2. Materials and methods

2.1 Materials

All chemicals were used as obtained without any additional purification. Cobalt nitrate hexahydrate ($Co(NO_3)_2 \cdot 6H_2O$), ferric nitrate hexahydrate ($Fe(NO_3)_3 \cdot 9H_2O$), citric acid ($C_6H_8O_7 \cdot H_2O$), ethylene glycol ($C_2H_6O_2$), ammonia ($NH_3 \cdot H_2O$), deionized water (DIW), MWCNT, melamine, and nitric acid (HNO_3) were sourced from Loba Chemie India, SRL, and Sigma-Aldrich and used for the synthesis of materials.

2.2 Synthesis of the $CoFe_2O_4$/g-C_3N_4/MWCNT nanocomposite

$CoFe_2O_4$ (CGC1) NPs were produced using the sol–gel autocombustion approach. Briefly, stoichiometric amounts of $Co(NO_3)_2 \cdot 6H_2O$, $Fe(NO_3)_3 \cdot 9H_2O$, and citric acid were individually dissolved in DIW. The metal nitrates were added to the stirred aqueous solution of citric acid, and the mixture was heated to 60 °C and stirred for 3 h. Then, ammonia was added to the solution to adjust the pH to 10. Further, the solution was heated to 60 °C for 4 h, and 20 mL of ethylene glycol was mixed. Once the solution turns into a black gel, the temperature is raised to 100 °C, at which point it undergoes self-propagating combustion. Finally, the obtained black powder was ground for 5 h at 700 °C to obtain a fine powder.

The synthesis of g-C_3N_4 was conducted through a direct pyrolysis of melamine. Initially, melamine was crushed. Then, the crushed melamine powder was placed in a crucible with a lid. The crucible was heated to 550 °C ± 5 °C at 10 °C min^{-1} in a muffle furnace (4 h). The resulting powder was yellowish and cleaned with HNO_3. Lastly, the obtained powder was dried in a hot-air oven (60 °C).

The ternary $CoFe_2O_4$/g-C_3N_4/MWCNT nanocomposite was fabricated employing the calcination approach, as shown in Table 1. Briefly, for the synthesis of $CoFe_2O_4$ + MWCNT (CGC2),

Table 1 Weight of each component in the sample for the fabrication of the nanocomposites

Abbreviation	$CoFe_2O_4$	MWCNTs	g-C_3N_4
CGC1	3 g	0	0
CGC2	3 g	0.15 g	0
CGC3	3 g	0	0.15 g
CGC4	3 g	0.15 g	0.15 g

3 g of $CoFe_2O_4$ and 0.15 g of MWCNT were mixed uniformly employing a mortar and pestle and annealed at 400 °C for 4 h. Similarly, for synthesizing $CoFe_2O_4$ + g-C_3N_4 (CGC3), 3 g of $CoFe_2O_4$ and 0.15 g of g-C_3N_4 were mixed and calcined at 400 °C for 4 h. The fabrication of $CoFe_2O_4$ + g-C_3N_4 + MWCNT (CGC4) involves the mixing of 3 g of $CoFe_2O_4$, 0.15 g of g-C_3N_4, and 0.15 g of MWCNT in a mortar and pestle, followed by calcination at 400 °C for 4 h.

2.3 Photocatalytic activity

The photocatalytic studies were performed in visible light using a 350 W xenon lamp. A standard method was used to produce a solution containing 10 ppm of the pollutant and 25 mg of the catalyst, yielding a final volume of 100 mL. A volume of 3–4 mL from the solution was subsequently obtained and designated as the initial concentration. The generated solutions are agitated in the dark for 30 min to attain the adsorption–desorption equilibrium. The mixture was later subjected to visible light. During irradiation, a volume of 4–5 mL of the suspension was collected at regular time intervals. Thereafter, the absorbance of the resulting supernatant was measured using a UV-Vis spectrophotometer after filtration.

3. Results and discussion

3.1 Synthesis of the composite and its characterization

3.1.1. Textural characterization (XRD and FESEM). Fig. 1(a and b) illustrate the XRD patterns of CGC1 ($CoFe_2O_4$), CGC2 ($CoFe_2O_4$ + MWCNT), CGC3 ($CoFe_2O_4$ + gC_3N_4), GC4 ($CoFe_2O_4$ + MWCNT + gC_3N_4), GCN and MWCNT. The XRD patterns of CGC1, CGC2, CGC3, and CGC4 match well with the JCPDS card no. 22-1086, which is associated with the diffraction pattern of pristine $CoFe_2O_4$ with a mixed spinel structure and $Fd\bar{3}m$ space group. A shift in the diffraction peaks in Fig. 1(a) is observed for all the composite samples in comparison to the original sample. The nanocomposites still retain the same spinel structure as $CoFe_2O_4$. This change occurs because the $CoFe_2O_4$ nanoparticles and the carbon nitride matrix interact very strongly, leading to some lattice distortion in the $CoFe_2O_4$ nanoparticles. The diffraction peaks are in positions, which mean the distance between the layers of atoms is different. This occurs because the atoms are not perfectly aligned, which causes strain and defects in the CGC composites during fabrication. The Williamson–Hall analysis in Fig. 1(c and d) also shows lattice strain in the CGC composites, as expected. The CGC composites undergo structural changes during their fabrication, affecting the lattice of $CoFe_2O_4$ nanoparticles.

The average crystallite size, lattice parameters, and strain were calculated using Scherrer's formula, Nelson–Riley plots, and Williamson–Hall plots, as given in Table 2.[35]

The FESEM images in Fig. 2 show the morphology of pure cobalt ferrite nanoparticles (CGC1) as densely agglomerated grains. For CGC2, a flake-like morphology is observed, whereas for CGC3, a sheet-like morphology is observed. Ferrite particles can be observed on the surfaces of these structures. In CGC2, layered aggregates are bridged by smoother surfaces that are consistent with the MWCNT bundles in CGC1 nanoparticles, providing an interconnected network that enhances charge transfer.[36]

CGC3 exhibits a sheet-like morphology with relatively flat surfaces, characteristic of stacked g-C_3N_4 layers on ferrite NPs. The sheet-like morphology enhances interfacial contact between g-C_3N_4 and cobalt ferrite NPs, thereby facilitating heterojunction formation and charge separation.[37]

CGC4 exhibits a clustered, flake-like morphology, with roughly spherical $CoFe_2O_4$ NPs on the surface of g-C_3N_4, interconnected by a conductive MWCNT carbon network at the semiconductor interfaces. The EDS spectra presented in Fig. S1 confirm the incorporation of carbon and nitrogen into cobalt ferrite from CGC1 to CGC4. CGC4 contains the highest carbon and nitrogen content, confirming the formation of a ternary $CoFe_2O_4$-MWCNT-g-C_3N_4 nanocomposite.

3.1.2. Chemical composition and nature of active sites (zeta potential, XPS, IR spectroscopy, and UV-Vis spectroscopy). Crystallite size and the lattice parameters increased with the incorporation of GCN and MWCNT in $CoFe_2O_4$. Also, there is a significant decrease in strain, which may be due to $CoFe_2O_4$ NPs, which exhibit substantial lattice strain arising from their high surface-to-volume ratio and crystal lattice defects. However, the introduction of g-C_3N_4 and MWCNT relieved the crystallographic stress. Fig. S2 shows the zeta potential of all the synthesized samples, revealing good colloidal stability of the nanoparticles in aqueous media.

XPS was utilized for the identification of surface chemical states and electronic interactions between CGC1 ($CoFe_2O_4$), CGC2 ($CoFe_2O_4$ + MWCNT), CGC3 ($CoFe_2O_4$ + g-C_3N_4), and CGC4 ($CoFe_2O_4$ + MWCNT + g-C_3N_4) composites, as illustrated in Fig. 3. The Co 2p spectra of all samples exhibit characteristic Co $2p_{3/2}$ and Co $2p_{1/2}$ spin–orbit doublets, accompanied by shake-up satellite signals, thereby confirming the existence of mixed Co^{2+}/Co^{3+} states typical of spinel $CoFe_2O_4$. In CGC1, the Co $2p_{3/2}$ peaks at 780.75 and 782.56 eV, and the Co $2p_{1/2}$ signals at 796.47 and 798.29 eV confirm the formation of inverse spinel cobalt ferrite. When MWCNTs and/or g-C_3N_4 are added, these peaks gradually move to the left. CGC2, CGC3, and CGC4 show Co $2p_{3/2}$ peaks near 779.34, 779.33, and 779.11 eV, and Co $2p_{1/2}$ peaks near 794.59, 794.77, and 794.13 eV, respectively. This shows strong electronic coupling and charge redistribution between ferrite and the carbonaceous matrices.

The Fe 2p spectra confirm the presence of both Fe^{3+} and Fe^{2+} species. For CGC1, the Fe $2p_{3/2}$ and Fe $2p_{1/2}$ doublets are centered at 710.49/724.88 eV (Fe^{3+}) and 711.98/726.40 eV (Fe^{2+}). For the composites, the binding energies shift slightly toward lower values, indicating that electrons can move more readily and that the redox capability increases due to interactions at the interface.

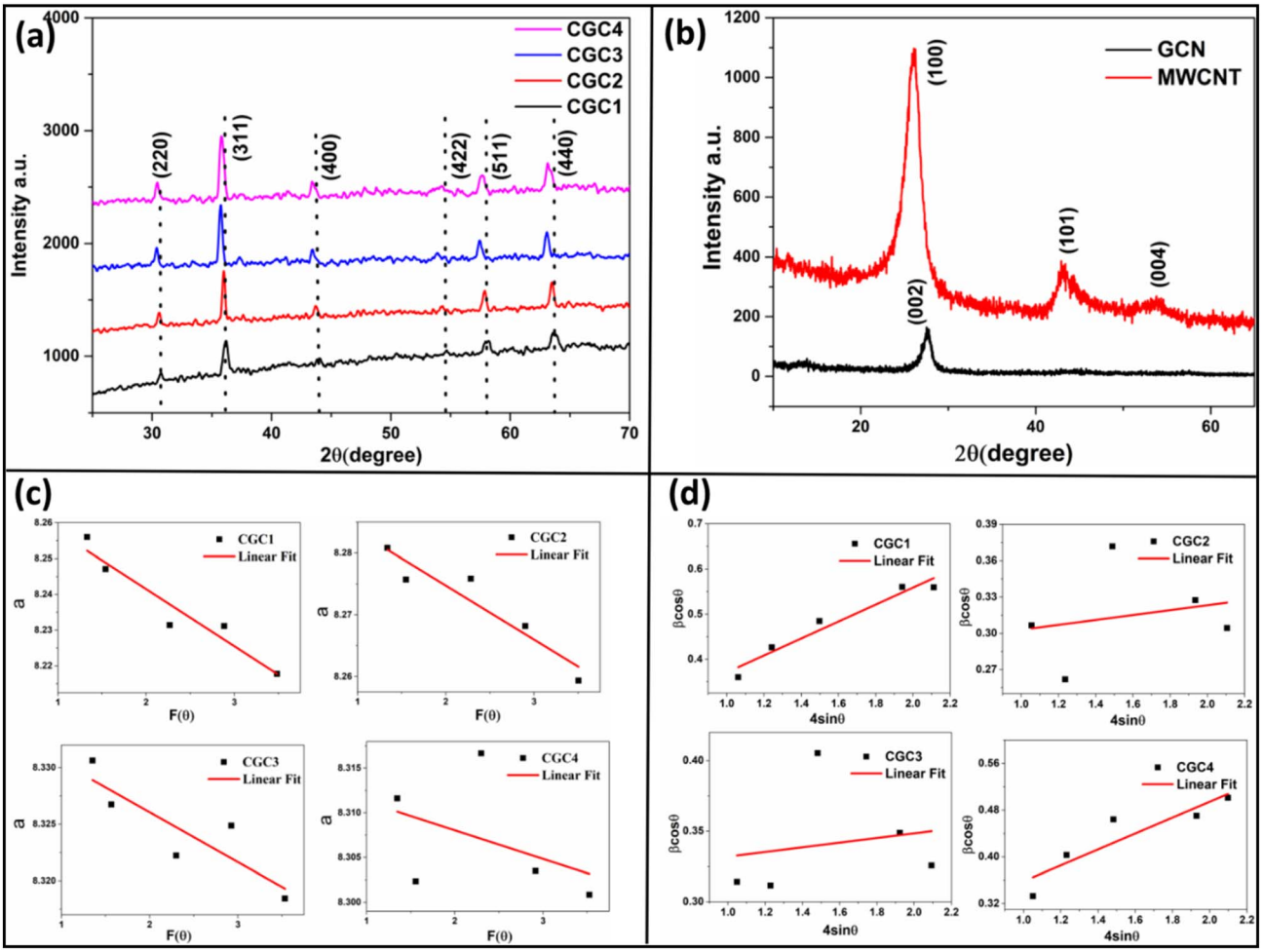

Fig. 1 XRD patterns of (a) pure and MWCNT, g-C_3N_4-modified $CoFe_2O_4$ NPs and (b) GCN and MWCNT. (c) Nelson–Riley plots and (d) W–H plots of pure and MWCNT, g-C_3N_4-modified $CoFe_2O_4$ NPs.

The O 1s spectra can be broken down into lattice oxygen (Co–O/Fe–O) and surface/defect oxygen components. CGC1 exhibits peaks at 531.36 and 533.38 eV, while CGC2 and CGC3 exhibit lattice oxygen at ~529–528 eV and defect oxygen at ~532–531 eV. CGC4 has three O 1s components at 528.36, 531.11, and 533.56 eV, indicating that it contains the most oxygen-vacancy-related and surface-active oxygen species. The systematic shifts in binding energy and the higher levels of defect oxygen in the ternary composite show that $CoFe_2O_4$, MWCNT, and g-C_3N_4 are strongly coupled. This is expected to improve charge transfer and catalytic and electrochemical performance.

The FTIR spectra of CGC1–CGC4 clearly show the formation of spinel $CoFe_2O_4$ and that MWCNT and g-C_3N_4 were successfully added to the composite systems, as seen in Fig. 4. CGC1 (pure $CoFe_2O_4$) exhibits a robust absorption band in the low-wavenumber range of 560–590 cm^{-1}. This band is typical of metal–oxygen (Fe–O/Co–O) stretching vibrations at the tetrahedral sites of the spinel ferrite lattice, which shows the formation of $CoFe_2O_4$. In CGC2 ($CoFe_2O_4$ + MWCNT), the metal–oxygen vibration is still present, but new bands appear in the higher wavenumber range, especially between 1580 and 1630 cm^{-1}. These new bands are due to the C=C stretching vibration of sp^2-hybridized carbons in the graphitic structure of MWCNTs.

The weak bands in the 1000–1200 cm^{-1} range are owing to the C–O stretching of surface oxygenated functional groups.

Table 2 Structural parameters of the pristine sample and nanocomposites

Parameters	CGC1	CGC2	CGC3	CGC4
Crystallite size (nm)	17.85 ± 3.48	26.75 ± 3.38	24.57 ± 2.55	19.53 ± 3.32
Lattice parameter '*a*' (Å)	8.273 ± 0.006	8.292 ± 0.004	8.334 ± 0.003	8.314 ± 0.009
Strain (ε)	0.189 ± 0.04	0.0203 ± 0.05	0.016 ± 0.04	0.136 ± 0.03
Zeta potential (mV)	−15.2	−12.8	−14	−13.3

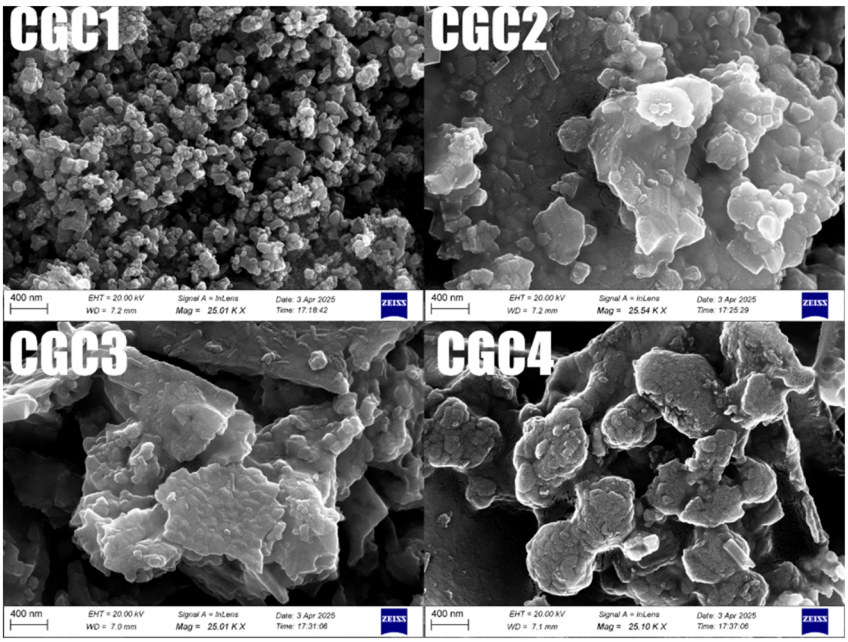

Fig. 2 FESEM images of CGC1, CGC2, CGC3 and CGC4.

These changes show that the MWCNTs and the ferrite matrix were successfully combined. In addition to the ferrite metal–oxygen band, CGC3 ($CoFe_2O_4$ + g-C_3N_4) exhibits an extensive range of absorption peaks between 1200 and 1650 cm^{-1}. These signals are caused by C–N and C=N stretching vibrations of the conjugated heptazine/triazine units of g-C_3N_4. There is also a characteristic band near 805–815 cm^{-1} that corresponds to the breathing mode of the tri-*s*-triazine rings, which shows the presence of graphitic carbon nitride. In the ternary composite CGC4, all these characteristic bands are observed simultaneously. The slight broadening and small shifts of the bands, especially in the metal–oxygen and carbon-related areas, suggest that $CoFe_2O_4$, MWCNTs, and g-C_3N_4 interact strongly with each other. These interactions indicate the formation of a well-integrated hybrid network, thereby improving charge transfer.

UV-visible spectroscopy was applied to analyze the optical properties of the fabricated nanomaterials. The Tauc plots for the synthesized samples, derived from UV-visible absorbance spectra, are presented in Fig. 5(a–c). The band gap energies were 2.51 eV for GCN, 1.62 eV for CGC1, and 2.66 eV for CGC4, respectively.

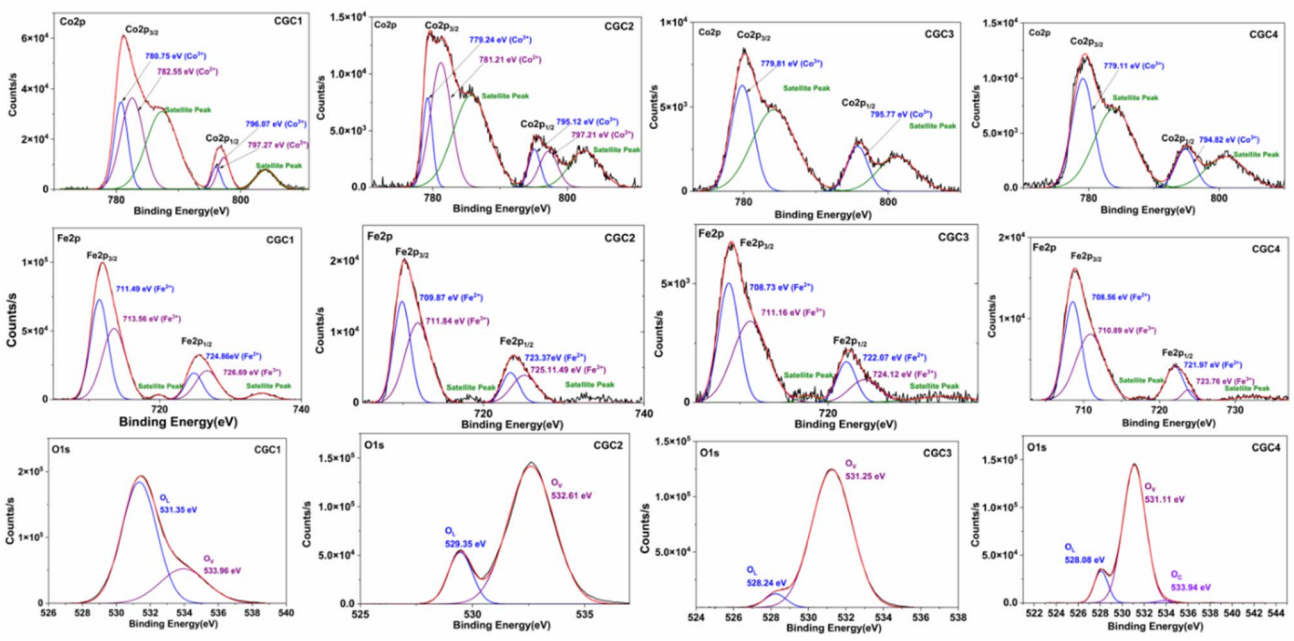

Fig. 3 XPS spectra of pure and MWCNT, g-C_3N_4-modified $CoFe_2O_4$.

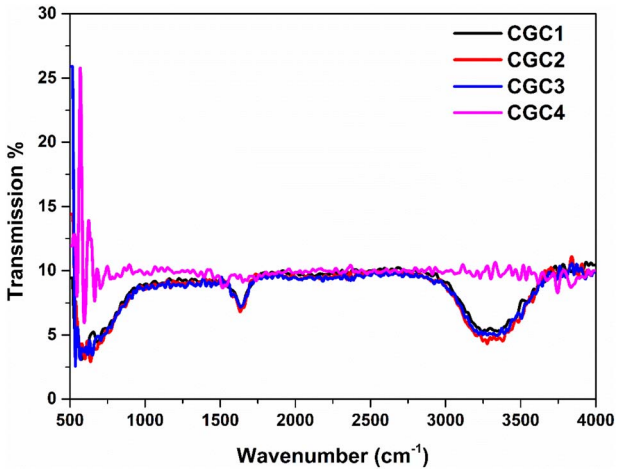

Fig. 4 FTIR spectra of pure and MWCNT, g-C_3N_4-modified $CoFe_2O_4$.

The diminished E_g values result from intensified electronic interactions between the semiconductor and MWCNTs, which facilitate charge separation. The amalgamation of materials with diverse energy levels alters the conduction and valence bands, hence reducing the band gap.[19] The decrease in band gap markedly improves photocatalytic efficacy by augmenting the light-harvesting efficiency.[19]

3.1.3. Electrochemical analysis

3.1.3.1. Cyclic voltammetry. To determine the electrochemical characteristics of all the samples, a CH Instruments three-electrode workstation was used, with Ag/AgCl as the reference electrode, a platinum wire as the counter electrode, and a glass carbon electrode as the working electrode. Cyclic voltammetry analysis is carried out for all the samples over the potential window of −1.5 V to 1.5 V at scan rates ranging from 0.8 V s^{-1} to 0.15 V s^{-1}, with a step size of 0.01 V s^{-1}. The study is carried out using ferri/ferrocyanide $[Fe(CN)_6^{3-/4-}]$ as a standard electrolyte. Fig. 6(a–d) shows the CV plots for all samples at diverse scan rates. It is observed that all the samples exhibit a pair of redox peaks, suggesting pseudocapacitive behavior.[38] At the same time, the composites, such as CGC2, CGC3, and CGC4, are hybrid materials that exhibit both pseudocapacitive and EDLC behavior. It is observed that, across all samples, the peak current increases with scan rate, indicating good rate capability.[39]

Even at the increased scan rate, the curve shape remains well-defined, indicating the outstanding electrochemical potential of the modified electrode. Further, the redox peaks are symmetric, and a very small shift is also observed, indicating the quasi-reversibility of redox reactions at the electrode surface.[40] The redox peaks observed in all the samples originate from the reversible electron transfer of the ferri/ferrocyanide redox probe, $[Fe(CN)_6^{3-/4-}]$.

For all samples, the electrode materials do not undergo chemical redox reactions but do influence the rate of electron transfer and the electroactive surface area. Further, the CGC2 sample exhibits the largest area under the curve, suggesting the highest charge-storage capability. This is due to the synergistic impact of MWCNTs and $CoFe_2O_4$ NPs, in which MWCNTs provide a conductive percolation network and improve interfacial electron transfer.[41] This improved charge storage capability is attributed to the highly stabilized interface and the synergistic effect, in which MWCNTs increase electron conductivity by providing a path to modify the volume.[41] CGC3 shows the second-best electrochemical properties due to the presence of $CoFe_2O_4$ NPs on graphitic carbon nitride. The electron cloud of g-C_3N_4 interacts with $CoFe_2O_4$ ions, thereby accelerating electron-transfer kinetics. $CoFe_2O_4$ NPs offer a high number of active sites, whereas g-C_3N_4 serves as a supporting agent, providing a high surface area and electronic conductivity.[42] This provides more active adsorption sites.[43,44] However, in CGC4, the presence of multiple interfaces increases the interfacial resistance and partially disrupts the CNT conductive network. Furthermore, the restacking of g-C_3N_4 nanosheets block the pores in CNTs, reducing electrolyte accessibility. This results in dilution of the electroactive ferrite fraction, thereby decreasing the number of available reaction sites. Therefore, the collective role of MWCNTs and g-C_3N_4 nanosheets results in

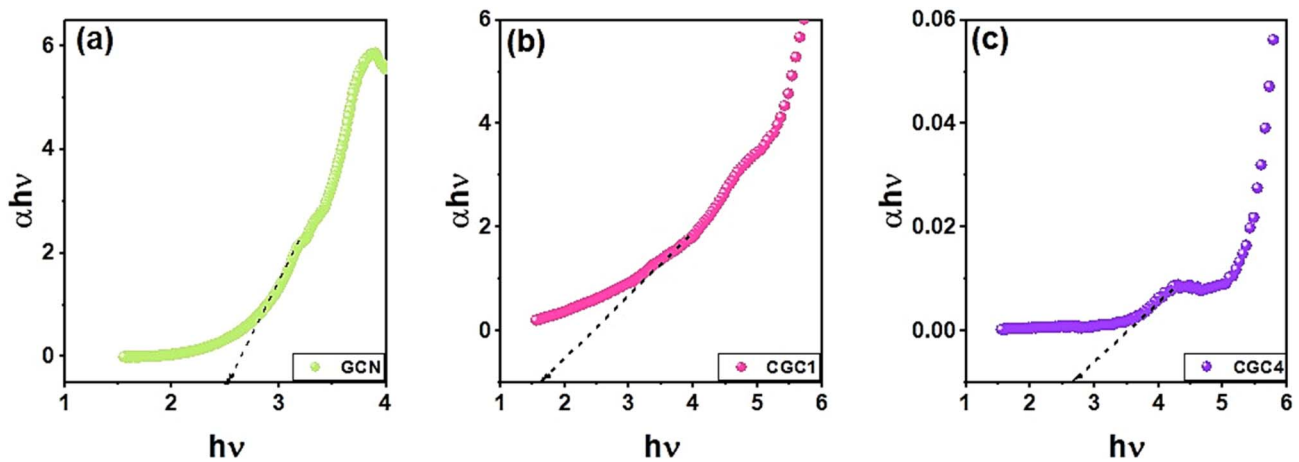

Fig. 5 Tauc plots of (a) GCN, (b) CGC1, and (c) CGC4.

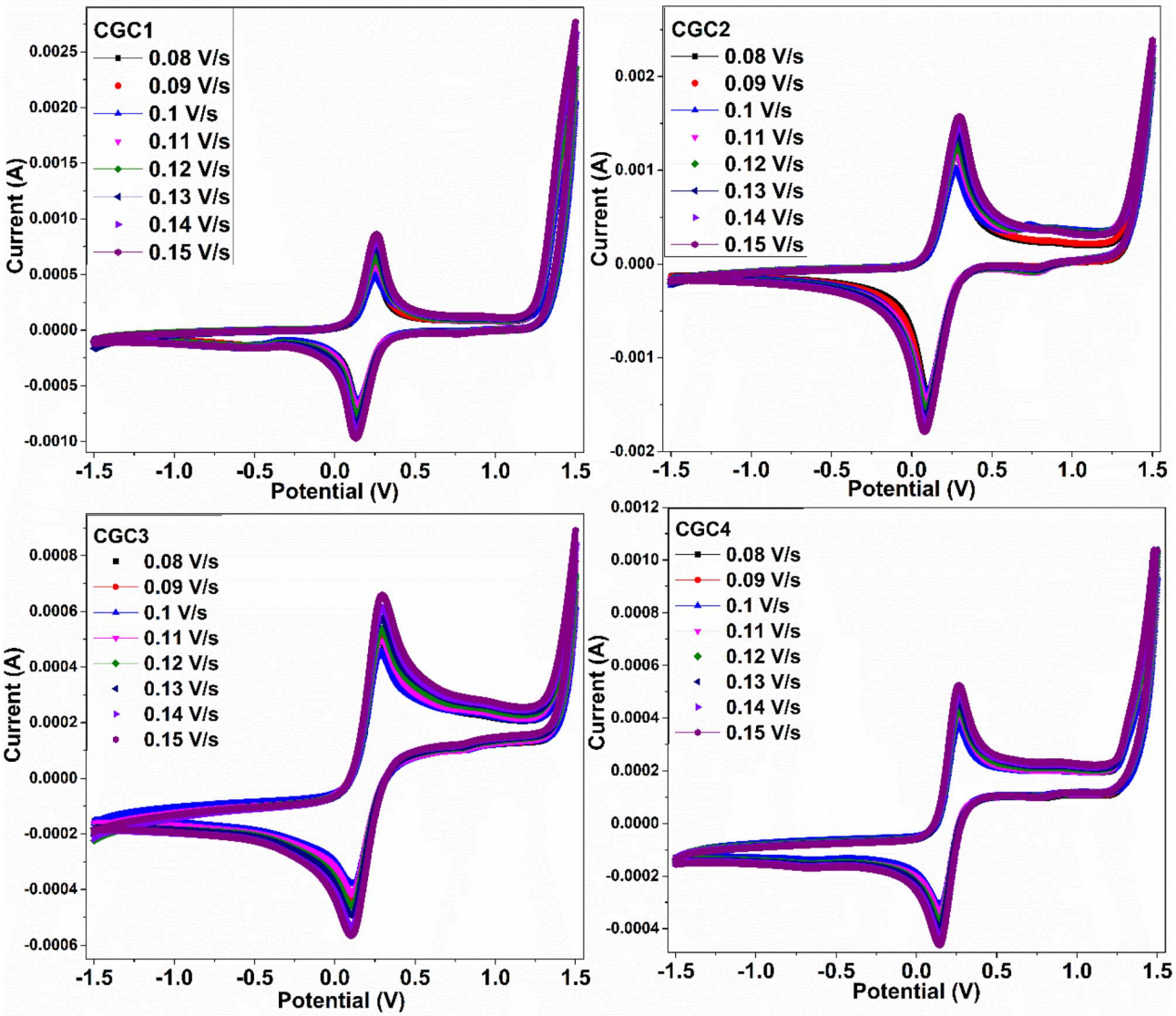

Fig. 6 CV curves of the prepared samples.

inferior electrochemical characteristics. Fig. 7 shows the Randles–Sevcik plots for the synthesized samples. The linear plot of peak current *vs.* scan rate suggests a diffusion-controlled process.[45] Furthermore, the higher slope observed for CGC2 and CGC3 indicates a larger electroactive surface area and enhanced ion diffusion compared to other samples. The CGC2 sample shows the highest diffusivity among all samples, consistent with the CV results.

3.1.3.2. Specific capacitance and other parameters. Fig. 8(a–d) shows the variation of specific capacitance (C_s), energy density (E), specific capacity (Q_s), and stored charge (q) for all the samples with respect to the scan rate. All parameters show a decreasing trend with increasing scan rate, attributed to their pseudocapacitive behavior and kinetic limitations at higher scan rates. The decrease in all parameters with increasing scan rate indicates that ions do not have enough time to access the inner layer of the active material at higher scan rates.[45] It is observed in Fig. 8(a) that the CGC2 sample shows a superior specific capacitance value when compared with other samples. This is attributed to a highly conductive network of MWCNTs, which facilitates rapid electron transport and reduces charge-transfer resistance. The tubular, porous structure of MWCNTs enhances electrolytic diffusion and exposes more electroactive sites, while simultaneously contributing to the electric double-layer capacitance.[46] Furthermore, CGC3 exhibits an intermediate specific capacitance, followed by CGC2. This is because of improved particle dispersion and surface wettability resulting from the presence of g-C_3N_4. However, the lower electrical conductivity of g-C_3N_4 compared to CNTs limits the performance of CGC3. It is also observed that the CGC4 sample unexpectedly shows the lowest specific capacitance. This can be attributed to the increased interfacial resistance and disruption of conductive pathways resulting from the combined effects of MWCNTs and g-C_3N_4.[47] A similar trend is observed across all parameters, such as E, Q_s, and q, with CGC2 showing the highest values and CGC4 the lowest, as shown in Fig. 8(b–d).

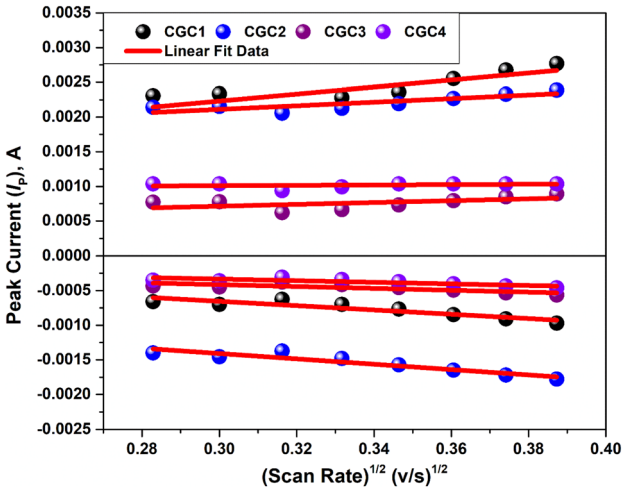

Fig. 7 Randles–Sevcik plots of the prepared samples.

The highest values for CGC2 are again due to improved electroactive surface area and ion accessibility, whereas the lowest values for CGC4 are due to increased interfacial resistance and mass dilution.

3.1.3.3. Electrochemical impedance spectroscopy and Bode plot. The Nyquist and Bode plots together provide a clear picture of ion transport and charge transmission characteristics of various samples. Fig. 9(a) displays the Nyquist plot for all the samples. It is observed that CGC1, CGC2, CGC3, and CGC4 demonstrate a combination of depressed semicircles at high frequencies and an inclined line at low frequencies. This indicates that both diffusion and interfacial charge transfer contribute to the overall impedance. The charge-transfer resistance, as measured by the semicircle diameter, is highest for CGC3 and lowest for CGC2, suggesting faster electron transfer in CGC2. The fast electron transfer kinetics are attributed to the highly conductive percolation network of MWCNTs in the CGC2 sample.[48] The CNTs provide a continuous pathway, reducing interfacial resistance. Although the CGC3 electrode exhibits the highest interfacial resistance, it still delivers higher capacitance than pristine ferrite owing to the improved electroactive surface area, enhanced wettability, and better dispersion of $CoFe_2O_4$ NPs on g-C_3N_4 sheets. In contrast, the ternary composite shows less resistance than CGC3 but the lowest capacitance, indicating that excessive structural complexity reduces electroactive

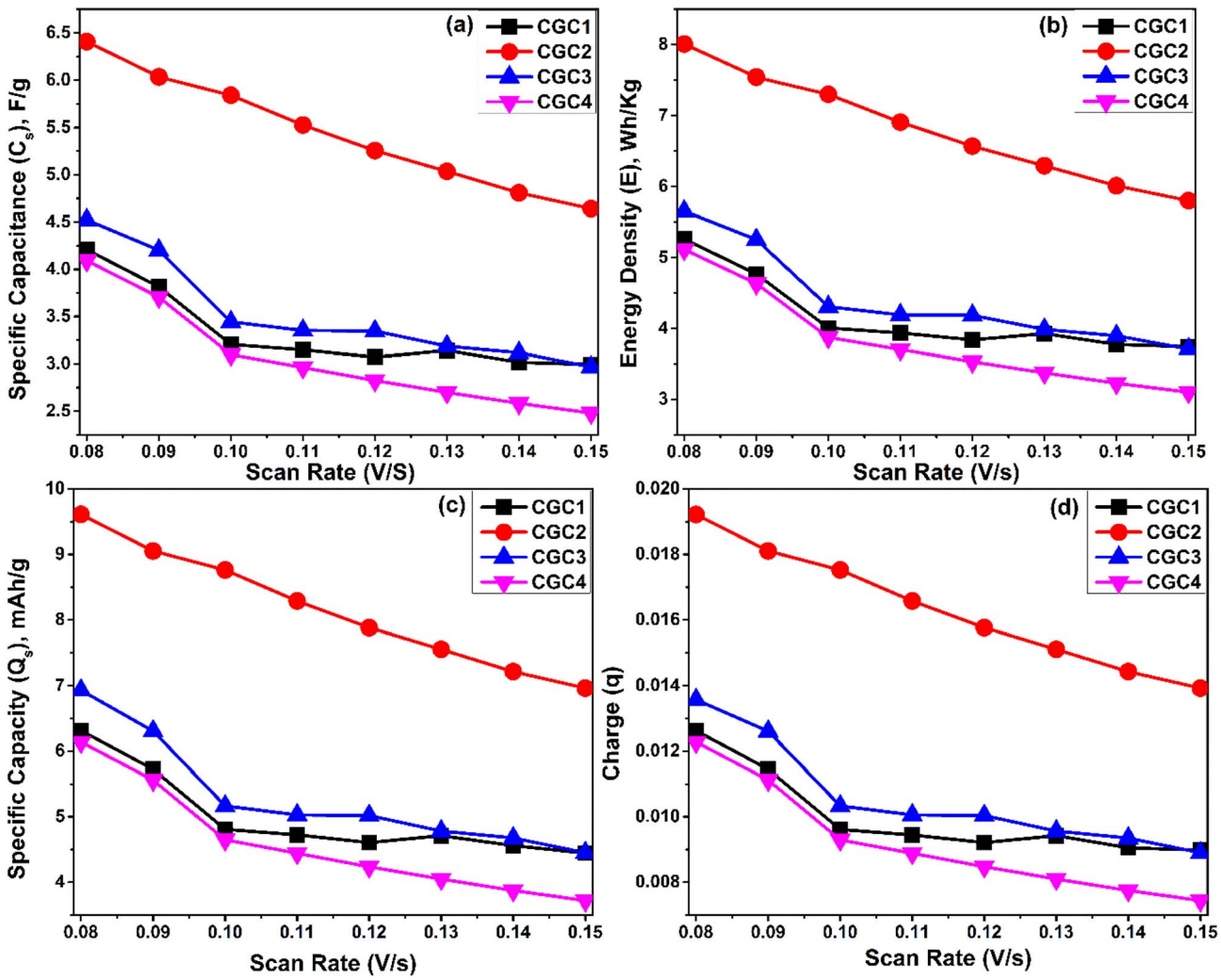

Fig. 8 (a) Specific capacitance, (b) energy density, (c) specific capacity, and (d) stored charge plots of CGC1, CGC2, CGC3, and CGC4.

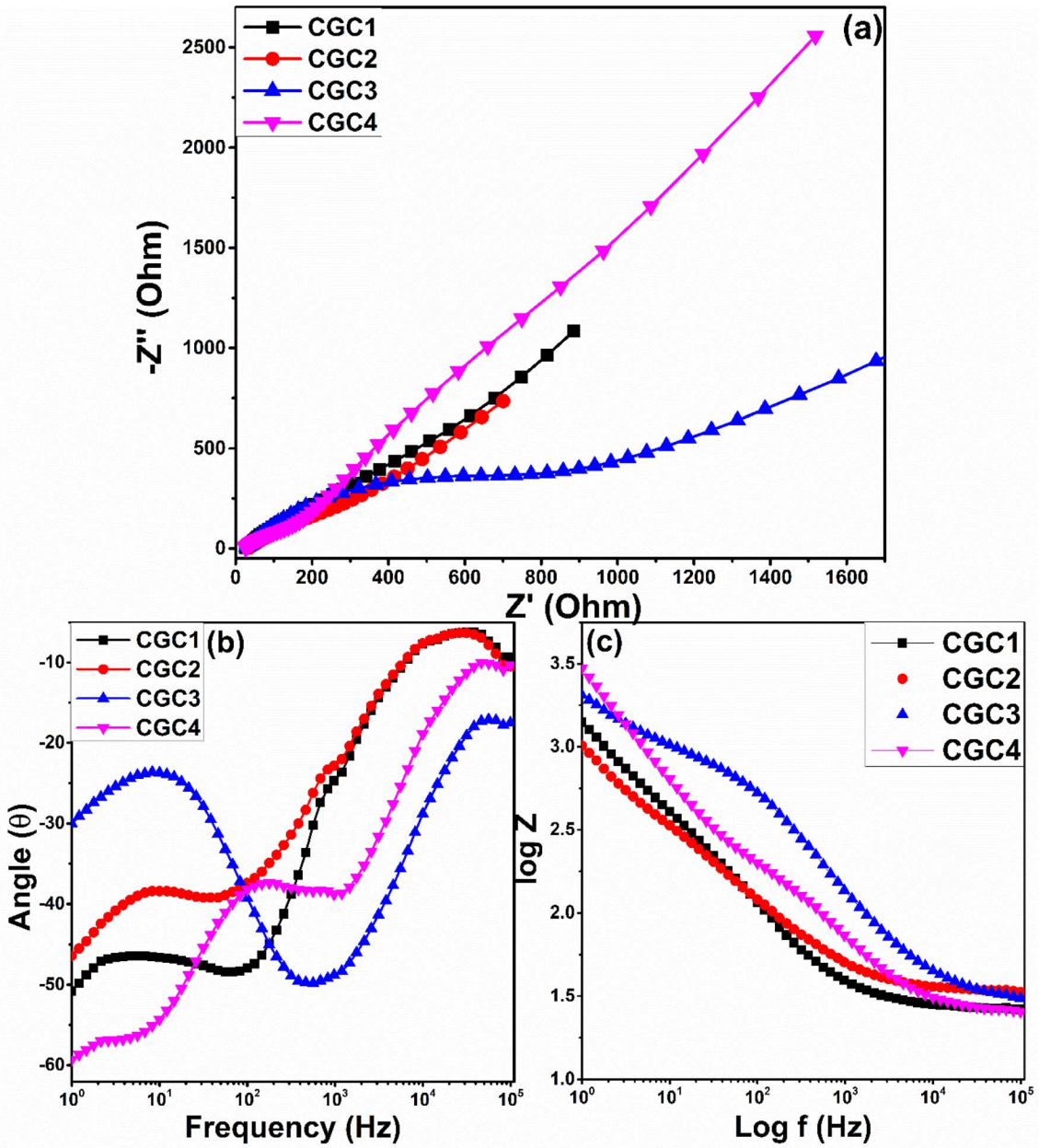

Fig. 9 (a) Electrochemical impedance spectra, (b) Bode phases, and (c) Bode magnitude plots of the prepared samples.

site utilization and introduces additional interfacial barriers. In the low-frequency region, the straight line corresponds to the Warburg impedance, which describes ion diffusion within the electrode pores.[49]

In this region, CGC4 shows the steepest slope, indicating rapid ion diffusion through the combined porous network of CNTs and layered g-C_3N_4.[50] Further, Fig. 9(b) shows the frequency-dependent dissimilarity in the Bode phase angle across all samples. Generally, a phase angle approaching −90° indicates good capacitive performance and an ideal charge–discharge process.[51] The Bode phase further supports the EIS analysis, in which CGC2 displays the highest phase angle. This indicates an ideal capacitive behavior owing to rapid electrochemical response and efficient charge storage. However, CGC3 shows the lowest phase angle, indicating a predominance of resistive behavior. A similar behavior is observed in the Bode magnitude plot, as displayed in Fig. 9(c). The impedance magnitude decreases with increasing frequency. This is a normal transition of ferrites from a resistive to the capacitive type.[52] However, it is again observed that CGC2 shows lower impedance than the other samples, suggesting improved electronic and ionic conductivity. However, despite efficient ion transport, the C_s value for this sample is the lowest, suggesting that ion diffusion alone does not govern charge storage.[53] Reduced electroactive sites, reduced electroactive mass fraction, and increased interfacial resistance overall limit the electrochemical performance of the electrode.

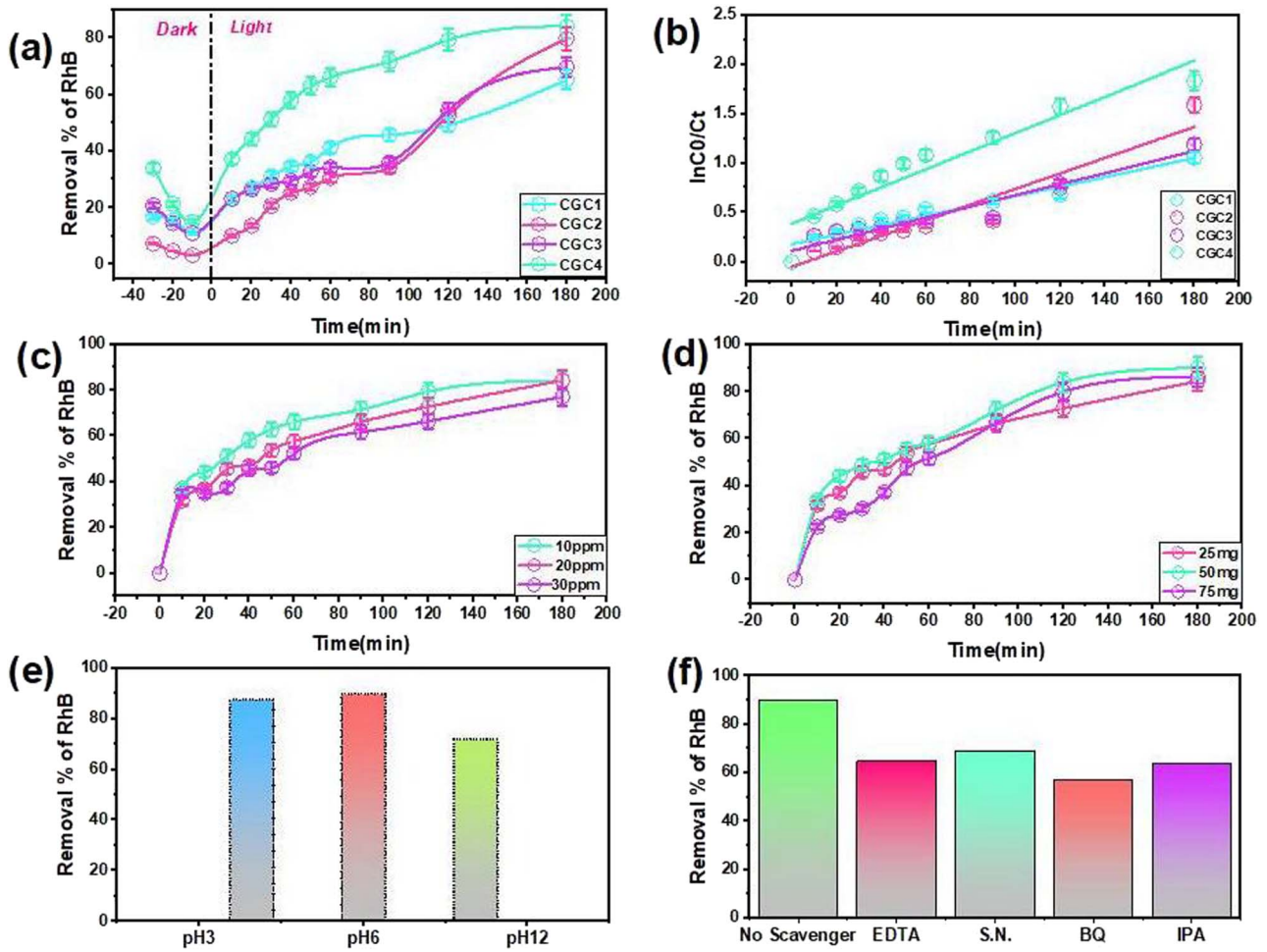

Fig. 10 (a) Photocatalytic decomposition of RhB using CGC1, CGC2, CGC3 and CGC4. (b) PFO kinetics curves. (c) Impact of RhB concentration on photodegradation efficiency. (d) Impact of CGC4 dosage on RhB degradation. (e) Impact of pH variation on photodecomposition. (f) Scavenging tests in the presence of EDTA, $AgNO_3$, IPA and BQ.

3.2 Photocatalytic activity

3.2.1. Photocatalytic decomposition of RhB. The photocatalytic performance of cobalt ferrite, incorporating MWCNTs and a g-C_3N_4 matrix, was assessed for the decomposition of an RhB solution. The photocatalytic effectiveness of the CGC1, CGC2, CGC3, and CGC4 catalysts was assessed by monitoring the decomposition of RhB under visible light. To attain this objective, an RhB pollutant solution at 10 ppm was prepared. A blank solution was produced to assess its absorbance. Afterward, 25 mg of the nanomaterials was added to the solution and incubated in the dark for 30 min to achieve equilibrium. Fig. 10(a) shows that after 30 min under dark conditions, the

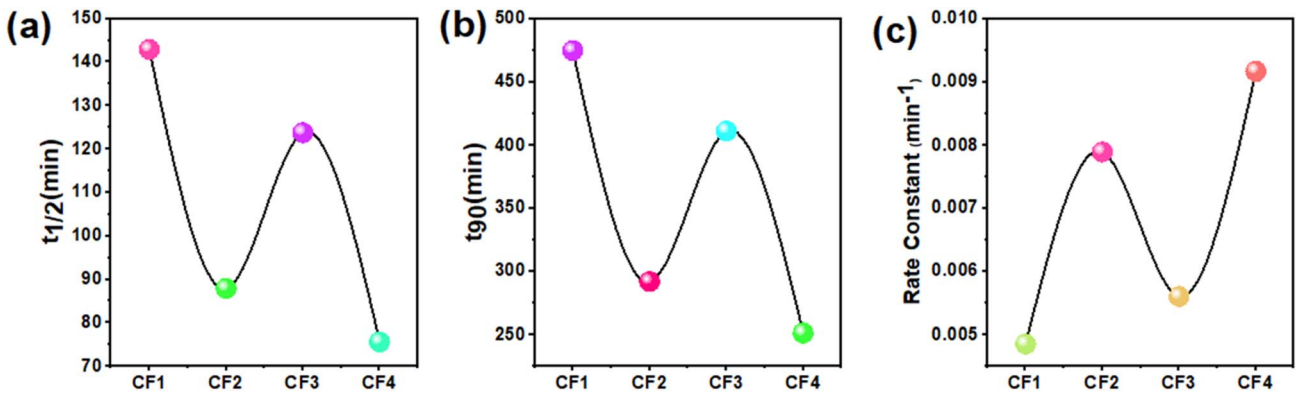

Fig. 11 (a) $t_{1/2}$, (b) t_{90}, and (c) rate constant plots of CGC1, CGC2, CGC3, and CGC4.

Table 3 Photocatalytic evaluation of the synthesized catalysts

Sample	Degradation (%)	K (s^{-1})	$t_{1/2}$ (min)	t_{90} (min)	R^2
CGC1	65.17	8.8×10^{-5}	142.9	474.7	0.928
CGC2	79.61	1.32×10^{-4}	87.8	291.8	0.922
CGC3	69.52	9.33×10^{-5}	123.7	411.1	0.930
CGC4	84.1	1.53×10^{-4}	75.5	251.1	0.900

system reached an adsorption–desorption equilibrium; however, the RhB conversion is approximately 33.8% under dark conditions for the CGC4 catalyst. Afterward, the samples were exposed to visible light, and the solution was removed every 10 min to measure its absorbance at C_t. Nevertheless, the removal efficiency of the CGC4 catalyst rises noticeably to 51.2% when exposed to visible light for 30 min. Adsorption plays a negligible part in the removal of RhB. A consistent pattern is observed in all the synthesized catalysts. The deterioration of RhB followed a progressive pattern, with CGC4 (84.1%) exhibiting the highest degradation rate, followed by CGC2 (79.6%), CGC3 (69.5%), and CGC1 (65.1%), after 180 min of visible light exposure. The enhanced capacity for degradation upon light exposure may be associated with the generation of a heterojunction among the three components. This heterojunction prevents elimination due to agglomeration and efficiently suppresses the recombination of photoinduced electrons and holes.[54] The influence of carbon nanotubes (MWCNTs) on photocatalytic activity was observed in CGC2 and CGC4 nanocomposite catalysts, especially noticeable in cobalt ferrite. A marked alteration in reaction rate was evident when cobalt ferrite NPs were deposited on the MWCNTs surface. The results indicate that incorporating MWCNTs substantially improves catalytic performance, likely due to synergistic interactions between MWCNTs and ferrite nanoparticles.[55] Table 4 presents a comparison of the efficacy of various photocatalysts for the degradation of RhB dye at different RhB concentrations and catalyst dosages.

The pseudo-first-order (PFO) kinetics equation was used to determine the rate constant, thereby improving our understanding of the efficacy of the synthesized photocatalysts. The equation is presented as follows:

$$\ln\frac{C_t}{C_0} = -kt \quad (1)$$

The variable k denotes the photodegradation rate, while C_0 and C_t denote the initial pollutant concentration and the concentration at time t, respectively.

The kinetics of RhB degradation, illustrated in Fig. 10(b), adhere to a pseudo-first-order reaction. The CGC4 catalyst exhibited an increased rate constant of 1.5×10^{-4}, significantly surpassing the rate constants of CGC1, CGC2, and CGC3, which were 8.8×10^{-5}, 1.3×10^{-4}, and 9.3×10^{-5}, respectively (Fig. 11(c)). The enhanced charge-carrier separation in CGC4 may account for the higher rate constant. The estimated factors are presented in Table 3. Using the rate constant, eqn (2) and (3) were utilized to determine the values for $t_{1/2}$ and t_{90}, respectively, as follows:

$$t_{1/2} = \frac{\ln(2)}{k}, \quad (2)$$

$$t_{90} = \frac{\ln(10)}{k}, \quad (3)$$

where t_{90} represents the duration required for 90% of the contaminant to degrade, while $t_{1/2}$ indicates the time necessary for 50% of the contaminant to decompose (Fig. 11(a and b)). Additionally, the influence of diverse photocatalytic conditions on photocatalytic activity was thoroughly examined. The CGC4 catalyst with the highest rate constant is selected for additional optimization of reaction variables based on the observed results.

3.2.2. HPLC analysis. The intermediates generated during the photodegradation of RhB were analyzed using HPLC, with findings depicted in Fig. 12(a–d). Given the potential spectral overlap between the parent dye and its decomposition products, HPLC acts as an additional approach to UV-Vis spectrophotometry for elucidating reaction kinetics and intermediates generated during the photocatalytic reaction. Fig. 12(a) depicts the overlay HPLC chromatograms of the RhB decomposition reactions recorded before the illumination treatment, and those after the complete decomposition after 180 min are shown in Fig. 12(b–e). The absorbance peak of pure RhB was detected at a retention period of 6.822 minutes on HPLC.

The intensities of the new peaks at designated retention times in the spectra decreased with an irradiation duration of

Table 4 Comparison of RhB dye degradation using different nanomaterials

Catalysts	Dye concentration (ppm)	Dosage concentration (mg)	Removal efficacy (%)	Time (min)	Ref.
Ce-doped ZnO	25	50	85.1	125	64
Ag–ZnO	5	20	66	120	65
$DyBa_2Fe_3O_{7.988}/DyFeO_3$	—	50	72	120	66
Bi_2S_3/Bi_2MoO_6	4.8	100	77.2	120	67
Bi_2S_3/CuS	10	100	55	300	68
N-Doped BiO/OVs-$BiVO_4$	10	50	69	240	69
rGO/$BiVO_4$	5	100	59	480	70
CGC4	**20**	**50**	**89.9**	**120**	**Present work**

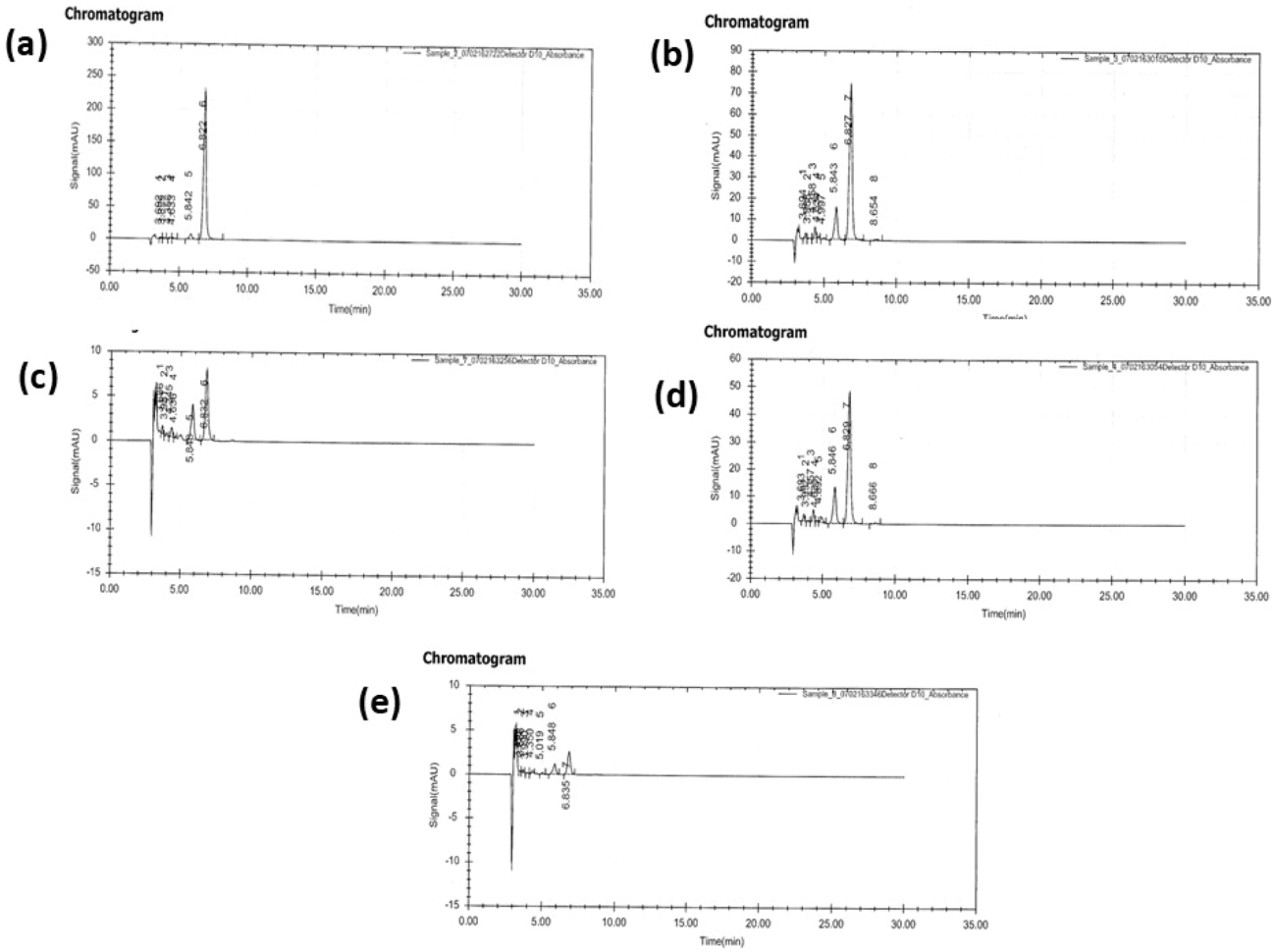

Fig. 12 HPLC analysis of RhB (a) without the catalyst and in the presence of (b) CGC1, (c) CGC2, (d) CGC3, and (e) CGC4 catalysts.

180 min, signifying the degradation efficacy of RhB for all intermediates, which encompass *N*,*N*-diethyl-*N*′-ethylrhodamine, *N*,*N*-diethylrhodamine, *N*-ethyl-*N*′-ethylrhodamine, *N*-ethylrhodamine, and rhodamine.[56] Additionally, several new peaks appeared during the reaction, which continued for 180 min. These peaks were expected to represent highly polar components, likely small-molecule intermediates.[57] It was also observed that the intensity of the RhB peak decreased and then decreased further after 180 min of the photocatalytic decomposition process. The decrease in the intensity of intermediate compounds further confirms that no harmful final products were formed.[58] Overall, the HPLC results strongly suggest that RhB can be effectively degraded and mineralized *via* photocatalysis.

3.2.3. Impact of reaction parameters. The optimization of several operational parameters essential for the degradation phenomena involved analyzing the impacts of catalyst dosage, drug concentration, and pH on direct current decomposition (under visible light exposure) using the CGC4 catalyst. Fig. 10(d) shows the impact of catalyst dosage on the performance of photodegradation. The elimination efficiency of CGC4 increases with catalyst dose (25–75 mg) and reaches a maximum at 50 mg. The lower removal efficiency at higher catalyst doses can be attributed to particle aggregation, which decreases the number of active sites.[59] Moreover, an increased catalyst dosage increases the turbidity of the solution, which can hinder light penetration and thereby reduce the degradation rate.

The impact of dye concentration is examined for the catalyst, CGC4, at a fixed dose of 50 mg. The elimination effectiveness as a function of dye concentration is presented in Fig. 10(c). The dye concentration is adjusted to 10–30 mg L^{-1}. The optimum elimination effectiveness is achieved at a dye concentration of 20 mg L^{-1}. Nevertheless, as the RhB concentration increased, the degradation rate decreased due to the reduced availability of catalytic sites for RhB molecules.[60] The rate of decomposition increases with the number of accessible active sites on the supported catalyst, leading to a higher concentration of RhB molecules on the catalyst surface. Consequently, a concentration of 20 mg L^{-1} RhB was identified as the optimal level for conducting a photocatalytic degradation experiment.

Electrostatic interactions between the dye molecules and the catalyst surface substantially affect the photocatalytic performance of the catalyst. Changes in pH modify the surface charge of the catalyst by altering the redox potentials of the valence and conduction bands, thereby affecting interfacial charge transfer.[61] Adjusting the reaction pH is crucial for the decomposition

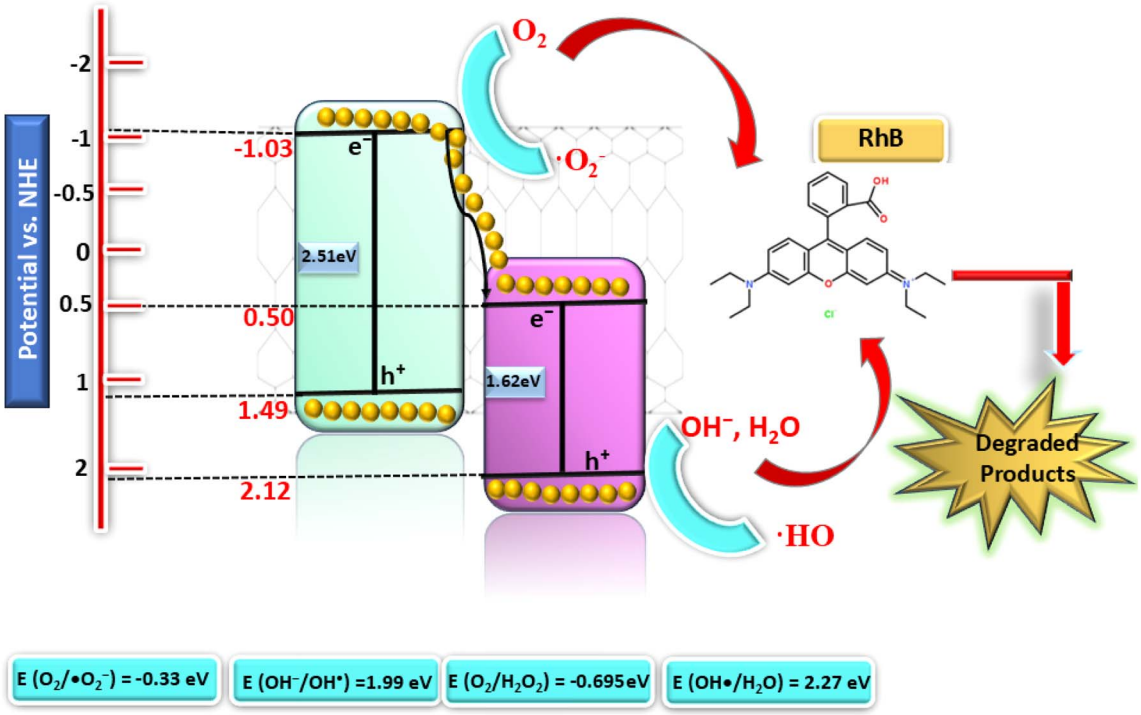

Fig. 13 Proposed mechanistic pathway of the Z-Scheme charge-transfer for RhB decomposition.

of contaminants, as it affects the surface charge of the catalyst. Consequently, it is imperative to analyze the behavior of pollutants at the active pH. Fig. 10(e) depicts the decomposition patterns of RhB at initial pH levels of 3, 6, and 12. The degradation efficiency increases with the initial pH of the RhB dye solution, rising from 87.5% at pH 3 to 89.9% at pH 6, then decreasing to 71.9% at pH 12. The decrease at higher pH levels may be associated with OH^- ions competing with RhB dye molecules for adsorption sites, thereby reducing RhB dye adsorption. Furthermore, excessive OH^- ions may engage with radicals ($^{\bullet}OH$), hence reducing the number of reactive species.[62] RhB removal was most efficient in robust acidic environments, followed by weak acidic environments. Our results corroborate prior evidence that acidic conditions favor RhB degradation.[63]

3.2.4. Degradation mechanism. To identify the active species in the decomposition reaction, RhB was degraded in the presence of scavengers, such as isopropyl alcohol (IPA), 1,4 benzoquinone (BQ), silver nitrate, and ethylenediaminetetraacetic acid disodium salt (EDTA), which scavenge $^{\bullet}OH$, $^{\bullet}O_2^-$, e^-, and h^+, respectively. Fig. 10(f) represents the impact of scavengers on the photo decomposition rate constant. The investigation indicates that the inclusion of BQ led to the lowest removal efficiency. Furthermore, the inclusion of IPA and EDTA led to a significant reduction in the removal efficiency. Silver nitrate does not significantly influence the rate constant, thereby eliminating the possibility of e^- as the active species. The inclusion of BQ, IPA, and EDTA indicates that $^{\bullet}OH$, $^{\bullet}O_2^-$, and h^+, radicals are the primary active species involved in the photodegradation process. These results can be readily elucidated using the information on band structures. As illustrated in Fig. 13, we propose a Z-scheme charge-transfer mechanism for decomposition, supported by scavenging tests and band-structure analysis *via* UV-visible absorbance spectroscopy. The band edge positions of the valence band (E_{VB}) and conduction band (E_{CB}) potentials of g-C_3N_4 and $CoFe_2O_4$ were determined using the following equations:

$$E_{CB} = \chi - E^e - E_g, \quad (4)$$

$$E_{VB} = E_g - E_{CB}, \quad (5)$$

where E_g is the band gap, χ is Mulliken's absolute electronegativity, and E^e is the energy of free electrons on the hydrogen scale (4.5 eV). For g-C_3N_4, the valence band (VB) and conduction band (CB) edge potentials were +1.49 eV and −1.03 eV, respectively, while for $CoFe_2O_4$, they were +2.12 eV and +0.50 eV, respectively. Visible light exposure facilitates the production of electrons (e^-) and holes (h^+) in the conduction band (CB) and valence band (VB) of the catalysts.[71] g-C_3N_4 possesses a loose, porous structure, thereby enhancing the availability of active sites for photocatalytic reactions. The photogenerated electrons are transmitted to MWCNTs, which serve as electron acceptors and transport conduits within the photocatalytic system.[72] The photogenerated electrons in the CB of cobalt ferrite preferentially migrate through the MWCNT network and recombine with holes in the VB of g-C_3N_4 because MWCNT has intimate interfacial contact and excellent electrical conductivity. The conduction band electrons at g-C_3N_4, with a more negative energy (−1.03 eV) than the standard reduction potential (−0.33 eV *vs.* NHE, $O_2/^{\bullet}O_2^-$),[73] facilitated the conversion of atmospheric oxygen into superoxide radicals. $CoFe_2O_4$ has a larger VB edge potential (2.12 eV) than $OH^-/^{\bullet}OH$ (1.99 eV) and

$H_2O/OH^{\bullet}$ (1.23 eV), allowing h^+ to oxidize OH^- and H_2O to produce $OH^{\bullet}$. Scavenging studies and band-structure analysis reveal that superoxide and hydroxyl radicals are the primary active species involved in the degradation of RhB.

4. Conclusion

This study successfully fabricated a ternary $CoFe_2O_4$/g-C_3N_4/MWCNT NC and systematically evaluated its efficacy in the visible-light-induced photocatalytic decomposition of RhB. The ternary CGC4 composite exhibited the highest photocatalytic performance (84.01%) and reaction rate constant (0.00917 min^{-1}) among the prepared catalysts. This was due to pseudo-first-order kinetics. The increased activity is due to a synergistic Z-scheme heterojunction mechanism that effectively suppresses electron–hole recombination, more efficiently utilizes light, and facilitates faster charge transfer at the interface. Parametric optimization showed that the amount of catalyst, dye concentration, and solution pH significantly affect degradation efficiency. Acidic conditions facilitate better removal of RhB. Radical-trapping experiments demonstrated that superoxide radicals and photogenerated holes are the primary agents in the degradation process. At the same time, HPLC analysis validated the gradual breakdown and mineralization of RhB, without the formation of persistent toxic intermediates. The electrochemical analysis revealed that the CGC2 electrode demonstrates superior performance, with a maximum C_s value of 6.407 F g^{-1}, an energy density of 8.008 W h kg^{-1}, and a specific capacity of 9.611 mAh h^{-1} at a scan rate of 0.08 V s^{-1}. However, the capacitance decreases with increasing scan rate, indicating diffusion-controlled processes. The superior performance of the CGC2 sample results from the synergistic effect of the conductive network of MWCNTs and the electroactive $CoFe_2O_4$ NPs.

Conflicts of interest

There are no conflicts to declare.

Data availability

Data will be made available upon request.

Supplementary information (SI) is available. See DOI: https://doi.org/10.1039/d6ra02055k.

References

1 Z. Chen, *et al.*, Water Eco-Nexus Cycle System (WaterEcoNet) as a key solution for water shortage and water environment problems in urban areas, *Water Cycle*, 2020, **1**, 71–77.
2 S. Khan, *et al.*, Emerging contaminants of high concern for the environment: Current trends and future research, *Environ. Res.*, 2022, **207**, 112609.
3 M. Mohammadi, *et al.*, Removal of rhodamine B from aqueous solution using palm shell-based activated carbon: adsorption and kinetic studies, *J. Chem. Eng. Data*, 2010, **55**(12), 5777–5785.
4 Y. Huang, *et al.*, Enhancement of rhodamine B removal by modifying activated carbon developed from Lythrum salicaria L. with pyruvic acid, *Colloids Surf., A*, 2016, **489**, 154–162.
5 K. Mahdavi, *et al.*, Enhanced photocatalytic degradation of toxic contaminants using Dy2O3-SiO2 ceramic nanostructured materials fabricated by a new, simple and rapid sonochemical approach, *Ultrason. Sonochem.*, 2022, **82**, 105892.
6 P. Zawadzki and M. Deska, Degradation efficiency and kinetics analysis of an advanced oxidation process utilizing ozone, hydrogen peroxide and persulfate to degrade the dye rhodamine B, *Catalysts*, 2021, **11**(8), 974.
7 W. Xiao, *et al.*, Preparation and evaluation of an effective activated carbon from white sugar for the adsorption of rhodamine B dye, *J. Clean. Prod.*, 2020, **253**, 119989.
8 P. Nuengmatcha, *et al.*, Visible light-driven photocatalytic degradation of rhodamine B and industrial dyes (texbrite BAC-L and texbrite NFW-L) by ZnO-graphene-TiO2 composite, *J. Environ. Chem. Eng.*, 2016, **4**(2), 2170–2177.
9 R. A. Nasr and E. A. Ali, Polyethersulfone/gelatin nanomembranes for the Rhodamine B dye removal and textile industry effluents treatment under cost effective condition, *J. Environ. Chem. Eng.*, 2022, **10**(2), 107250.
10 M. A. Younis, *et al.*, Molybdenum carbide nanosheets with iron doping as electrocatalysts for highly efficient ammonia electrosynthesis, *J. Electroanal. Chem.*, 2024, **975**, 118749.
11 J. Xu, *et al.*, Synergistic enhancement of visible-light photocatalysis in X/Fe3O4/AlON heterojunctions for efficient and recoverable dye degradation, *Ceram. Int.*, 2025, **52**(2), 2643–2653.
12 A. Ajmal, *et al.*, Principles and mechanisms of photocatalytic dye degradation on TiO 2 based photocatalysts: a comparative overview, *RSC Adv.*, 2014, **4**(70), 37003–37026.
13 S. Khan, *et al.*, Photocatalytic dye degradation from textile wastewater: a review, *ACS Omega*, 2024, **9**(20), 21751–21767.
14 S. Ma, *et al.*, CdS/Bi2S3 heterojunction for boosted photocatalysis *via* synergistic H2O adsorption and charge separation, *Int. J. Hydrogen Energy*, 2026, **229**, 154748.
15 Q. Xu, *et al.*, Direct Z-scheme photocatalysts: Principles, synthesis, and applications, *Mater. Today*, 2018, **21**(10), 1042–1063.
16 S. Dharani, *et al.*, Photodegrading rhodamine B dye with cobalt ferrite-graphitic carbon nitride (CoFe2O4/g-C3N4) composite, *Environ. Res.*, 2024, **258**, 119484.
17 M. F. Ehsan, *et al.*, CoFe2O4 decorated g-C3N4 nanosheets: New insights into superoxide anion mediated photomineralization of methylene blue, *J. Environ. Chem. Eng.*, 2020, **8**(6), 104556.
18 M. Abdel-Salam and T. Yoon, Cobalt-ferrite/Ag-fMWCNT hybrid nanocomposite catalyst for efficient degradation of synthetic organic dyes *via* peroxymonosulfate activation, *Environ. Res.*, 2022, **205**, 112424.
19 D. Varghese, *et al.*, *Synergistic design of CuO/$CoFe_2O_4$/MWCNTs ternary nanocomposite for enhanced photocatalytic*

degradation of tetracycline under visible light, *Sci. Rep.*, 2025, **15**(1), 320.

20 M. Gabal, *et al.*, CoFe2O4/MWCNTs nano-composites structural, thermal, magnetic, electrical properties and dye removal capability, *Mater. Res. Express*, 2019, **6**(10), 105059.

21 S. Vignesh, R. Mythili and T. H. Oh, Boosted photocatalytic performance of cobalt ferrite anchored g-C3N4 nanocomposite toward various emerging environmental hazardous pollutants degradation: insights into stability and Z-scheme mechanism, *Environ. Geochem. Health*, 2024, **46**(8), 302.

22 L. Jiang, *et al.*, Construction of an all-solid-state Z-scheme photocatalyst based on graphite carbon nitride and its enhancement to catalytic activity, *Environ. Sci.: Nano*, 2018, **5**(3), 599–615.

23 H. Wang, *et al.*, Novel strategy of defect-induced graphite nitride carbon preparation and photocatalytic performance, *Catal. Lett.*, 2018, **148**(5), 1296–1308.

24 B. Chai, *et al.*, Enhanced visible light photocatalytic degradation of Rhodamine B over phosphorus doped graphitic carbon nitride, *Appl. Surf. Sci.*, 2017, **391**, 376–383.

25 P. Hao, *et al.*, Recent advances, application and prospect in g-C3N4-based S-scheme heterojunction photocatalysts, *Sep. Purif. Technol.*, 2024, **330**, 125302.

26 A. Verma, *et al.*, Graphitic carbon nitride (g-C3N4)-based magnetic photocatalysts for removal of antibiotics, *Carbon Lett.*, 2025, **35**(1), 45–73.

27 J. Li, *et al.*, In situ formation of red/black phosphorus-modified SiO 2@ gC 3 N 4 multi-heterojunction for the enhanced photocatalytic degradation of organic contaminants, *RSC Adv.*, 2023, **13**(19), 13142–13155.

28 D. Jiang, *et al.*, Enhanced photocatalytic activity of graphitic carbon nitride/carbon nanotube/Bi2WO6 ternary Z-scheme heterojunction with carbon nanotube as efficient electron mediator, *J. Colloid Interface Sci.*, 2018, **512**, 693–700.

29 R. C. Pawar, *et al.*, Gold nanoparticle modified graphitic carbon nitride/multi-walled carbon nanotube (gC 3 N 4/ CNTs/Au) hybrid photocatalysts for effective water splitting and degradation, *RSC Adv.*, 2015, **5**(31), 24281–24292.

30 L. Harikrishnan, K. Alwar and A. Rajaram, Structural and morphological studies of g-C3N4-functionalized MWCNTs nanocomposite for sunlight-responsive photocatalytic activity, *Surf. Interfaces*, 2024, **54**, 105238.

31 A. Ahmed, *et al.*, Synthesis of visible-light-responsive lanthanum-doped copper ferrite/graphitic carbon nitride composites for the photocatalytic degradation of toxic organic pollutants, *Diamond Relat. Mater.*, 2024, **141**, 110630.

32 G. Gebreslassie, *et al.*, Direct Z-scheme CoFe2O4-loaded g-C3N4 photocatalyst with high degradation efficiency of methylene blue under visible-light irradiation, *Inorganics*, 2023, **11**(3), 119.

33 N. Chandel, *et al.*, Adsorption and photocatalysis compiled toxic dyes mineralization using graphitic carbon nitride modified ZnFe2O4 and CoFe2O4 photocatalysts supported onto N-doped graphene, *Desalin. Water Treat.*, 2020, **191**, 381–399.

34 S. N.-U.-Z. Haider, *et al.*, Z-scheme Bi2WO6/KCN heterojunction towards efficient photocatalytic degradation of tetracycline hydrochloride, *Mater. Today Sustain*, 2024, **27**, 100921.

35 M. F. Ahmed, *et al.*, Effect of calcination temperature on nano-cobalt ferrite synthesized by sol-gel method for modification of structural, morpholological, magnetic, electrical and optical properties, *Mater. Adv.*, 2025, **6**, 6724–6741.

36 S. Kumar, *et al.*, Hybrid structure of MWCNT/ferrite and GO incorporated composites for microwave shielding properties and their practical applications, *RSC Adv.*, 2021, **11**(17), 9775–9787.

37 S. Hassanzadeh, S. Farhadi and F. Moradifard, Synthesis of magnetic graphene-like carbon nitride-cobalt ferrite (gC 3 N 4/CoFe 2 O 4) nanocomposite for sonocatalytic remediation of toxic organic dyes, *RSC Adv.*, 2023, **13**(16), 10940–10955.

38 B. Rani and N. K. Sahu, Electrochemical properties of CoFe2O4 nanoparticles and its rGO composite for supercapacitor, *Diamond Relat. Mater.*, 2020, **108**, 107978.

39 Z. Chen, *et al.*, Design and synthesis of hierarchical nanowire composites for electrochemical energy storage, *Adv. Funct. Mater.*, 2009, **19**(21), 3420–3426.

40 J.-H. Kim, *et al.*, Microstructure and pseudocapacitive properties of electrodes constructed of oriented NiO-TiO2 nanotube arrays, *Nano Lett.*, 2010, **10**(10), 4099–4104.

41 M. Mumtaz, *et al.*, Nanohybrids of multi-walled carbon nanotubes and cobalt ferrite nanoparticles: High performance anode material for lithium-ion batteries, *Carbon*, 2021, **171**, 179–187.

42 X. B. Joseph, *et al.*, CoFe 2 O 4 supported gC 3 N 4 nanocomposite for the sensitive electrochemical detection of dopamine, *New J. Chem.*, 2021, **45**(38), 18131–18138.

43 D.-M. Kim, *et al.*, Two-dimensional nanocomposites based on tungsten oxide nanoplates and graphene nanosheets for high-performance lithium ion batteries, *Electrochim. Acta*, 2015, **163**, 132–139.

44 B. Talluri, *et al.*, Nanocomposites of digestively ripened copper oxide quantum dots and graphene oxide as a binder free battery-like supercapacitor electrode material, *Electrochim. Acta*, 2019, **321**, 134709.

45 S. Peng, *et al.*, Fabrication of spinel one-dimensional architectures by single-spinneret electrospinning for energy storage applications, *ACS Nano*, 2015, **9**(2), 1945–1954.

46 S. Ramesh, *et al.*, Electrochemical performance of MWCNT/GO/NiCo2O4 decorated hybrid nanocomposite for supercapacitor electrode materials, *J. Alloys Compd.*, 2018, **765**, 369–379.

47 S. Polat and D. Faris, Fabrication of CuFe2O4@ g-C3N4@ GNPs nanocomposites as anode material for supercapacitor applications, *Ceram. Int.*, 2022, **48**(17), 24609–24618.

48 O. Ibukun and H. K. Jeong, An activated carbon and carbon nanotube composite for a high-performance capacitor, *New Phys. Sae. Mulli*, 2018, **68**, 185–188.

49 A. N. Naveen and S. Selladurai, Investigation on physiochemical properties of Mn substituted spinel cobalt oxide for supercapacitor applications, *Electrochim. Acta*, 2014, **125**, 404–414.
50 M. M. Huq, C.-T. Hsieh and C.-Y. Ho, Preparation of carbon nanotube-activated carbon hybrid electrodes by electrophoretic deposition for supercapacitor applications, *Diamond Relat. Mater.*, 2016, **62**, 58–64.
51 A. Ghosh and Y. H. Lee, Carbon-based electrochemical capacitors, *ChemSusChem*, 2012, **5**(3), 480–499.
52 K. A. Alrashidi, *et al.*, Ultrafast Charge Storage in Y-Activated NiFe2O4 Nanoferrites ceramics For energy storage application, *Ceram. Int.*, 2026, **52**(5), 6577–6594.
53 A. Ali, *et al.*, Progress in cathode materials for rechargeable Zinc-Ion batteries: from inorganic and organic systems to hybrid frameworks and biomass-derived innovations, *Prog. Mater. Sci.*, 2025, 101543.
54 X. Zhang, *et al.*, Fabrication of hydrangea-shaped Bi2WO6/ZIF-8 visible-light responsive photocatalysts for degradation of methylene blue, *Chemosphere*, 2022, **307**, 135949.
55 C.-H. Chen, Y.-H. Liang and W.-D. Zhang, ZnFe2O4/MWCNTs composite with enhanced photocatalytic activity under visible-light irradiation, *J. Alloys Compd.*, 2010, **501**(1), 168–172.
56 F. Alfifi, *et al.*, Phytomediated chitosan-modified ZnO NPs for photocatalytic degradation of rhodamine B: Analytical insights through LC/MS and HPLC, *Inorg. Chem. Commun.*, 2025, 115771.
57 H. Fu, *et al.*, Photocatalytic degradation of RhB by fluorinated Bi2WO6 and distributions of the intermediate products, *Environ. Sci. Technol.*, 2008, **42**(6), 2085–2091.
58 T. Rasheed, *et al.*, TiO2/UV-assisted rhodamine B degradation: putative pathway and identification of intermediates by UPLC/MS, *Environ. Technol.*, 2018, **39**(12), 1533–1543.
59 N. Soltani, *et al.*, Visible light-induced degradation of methylene blue in the presence of photocatalytic ZnS and CdS nanoparticles, *Int. J. Mol. Sci.*, 2012, **13**(10), 12242–12258.
60 G. Rana, *et al.*, Phytomediated synthesis of Fe3O4 nanoparticles using Cannabis sativa root extract: photocatalytic activity and antibacterial efficacy, *Biomass Convers. Biorefin.*, 2025, **15**(7), 10275–10292.
61 M. Ahmad, *et al.*, Enhanced photocatalytic degradation of RhB dye from aqueous solution by biogenic catalyst Ag@ZnO, *J. Alloys Compd.*, 2022, **895**, 162636.
62 A. Nezamzadeh-Ejhieh and S. Moeinirad, Heterogeneous photocatalytic degradation of furfural using NiS-clinoptilolite zeolite, *Desalination*, 2011, **273**(2–3), 248–257.
63 A. V. Mohod, *et al.*, Degradation of Rhodamine dyes by Advanced Oxidation Processes (AOPs)–Focus on cavitation and photocatalysis-A critical review, *Water Resour. Ind.*, 2023, **30**, 100220.
64 Z. Shen, *et al.*, Facile synthesis of 3D flower-like mesoporous Ce-ZnO at room temperature for the sunlight-driven photocatalytic degradations of RhB and phenol, *J. Colloid Interface Sci.*, 2019, **556**, 726–733.
65 E. Ersöz and O. Altintas Yildirim, Green synthesis and characterization of Ag-doped ZnO nanofibers for photodegradation of MB, RhB and MO dye molecules, *J. Korean Ceram. Soc.*, 2022, **59**(5), 655–670.
66 M. A. Mahdi, *et al.*, Green synthesis of DyBa2Fe3O7. 988/DyFeO3 nanocomposites using almond extract with dual eco-friendly applications: photocatalytic and antibacterial activities, *Int. J. Hydrogen Energy*, 2022, **47**(31), 14319–14330.
67 X. Li, *et al.*, A controlled anion exchange strategy to synthesize Bi2S3 nanoparticles/plate-like Bi2WO6 heterostructures with enhanced visible light photocatalytic activities for Rhodamine B, *Ceram. Int.*, 2016, **42**(2), 3154–3162.
68 Z.-Q. Liu, *et al.*, Facile hydrothermal synthesis of Bi 2 S 3 spheres and CuS/Bi 2 S 3 composites nanostructures with enhanced visible-light photocatalytic performances, *CrystEngComm*, 2012, **14**(23), 8261–8267.
69 C. Lai, *et al.*, In-situ preparation of N-doped Bi0/OVs-BiVO4 photocatalysts with enhanced photocatalytic properties, *J. Alloys Compd.*, 2024, **972**, 172852.
70 S. Xiong, *et al.*, Preparation of a Leaf-Like BiVO4-Reduced Graphene Oxide Composite and Its Photocatalytic Activity, *J. Nanomater.*, 2017, **2017**(1), 3475248.
71 B. J. Khatibzdeha, N. Keramatib and M. M. Ghazia, Magnetically separable CoFe2O4/CuO photocatalyst for degradation of methylene blue under visible light, *J. Appl. Chem.*, 2020, **15**(57), 21–28.
72 J. Dreo and P. Siarry, Stochastic metaheuristics as sampling techniques using swarm intelligence, *SI: ACO/PSO*, 2007, 199–216.
73 R. K. Dharman and T. H. Oh, Fabrication of g-C3N4@N-doped Bi2MoO6 heterostructure for enhanced visible-light-driven photocatalytic degradation of tetracycline pollutant, *Chemosphere*, 2023, **338**, 139513.